COMBINING 4D HYPERSPECTRAL IMAGING WITH CNN FOR NERVE AND LIGAMENT DIFFERENTIATION

Naira Matosyan[a], Narek Chilingaryan[b*], Narine Sarvazyan[abc], Varduhi Yeghiazaryan[a]*

[a] American University of Armenia, Akian College of Science and Engineering, Yerevan, Armenia
[b] L. A. Orbeli Institute of Physiology NAS RA, Yerevan, Armenia
[c] George Washington University, Washington, DC, United States

ABSTRACT

Iatrogenic nerve injuries, inadvertently caused by an operating physician, occur at a significant annual rate. A major reason for such intraoperative damage is poor nerve visualization, which results in the transection of incorrect structures or the misidentification of nerves as vessels or ligaments. Previously, diffuse reflectance-based hyperspectral imaging (HSI) has been applied to the nerve differentiation issue in the surgical context. In contrast, our study addresses the task of differentiating between nerves and ligaments using 3D and 4D autofluorescence HSI, followed by classification using CNN and linear unmixing. Our experiments use excised bovine nerve and ligament samples. The data indicate that utilizing a 4D HSI configuration increases classification performance by up to 10%, achieving nearly 98.9% accuracy in most cases. Furthermore, CNNs consistently outperform linear unmixing, at times by more than 15%. We conclude that combining multiple autofluorescence HSI datacubes acquired at several narrow-band excitation wavelengths with a CNN approach enables superior differentiation between nerve and ligament samples. Our code is available at https://github.com/nairamatosyan/nerve-lig-4D-hsi-cnn.

***Index Terms*—** hyperspectral imaging, CNN, deep learning, linear unmixing, classification

1. INTRODUCTION

Iatrogenic nerve injuries (INI), meaning an injury caused by a physician [1], happen at a non-negligible rate in patients undergoing surgeries. In the US only, 400,000 to 600,000 INI cases are reported annually [2]. INIs can be classified into operative and non-operative types. The causes and mechanisms are diverse. They include but are not limited to: transecting nerves because they were not visualized, because they were not correctly identified, or they were taken for vessels. Extreme cases, when nerves have been used as grafts in place of tendons, have also occurred [1]. Current methods of addressing the INI problem rely either on electrophysiology-based intraoperative nerve monitoring (IONM), which can only detect the already-caused harm, or preoperative nerve visualizations, which cannot guide the surgeon in real-time [2].

Hyperspectral imaging (HSI) is a powerful technique allowing for contact-free substance characterization and differentiation based on its physicochemical properties and composition [3, 4]. According to a bibliometric investigation [5], the field is in an actively growing phase, in particular in the medical domain: diverse hardware and computational means are continuously developed for diagnostic, surgical and other medicine-related purposes. Hyperspectral images are typically three dimensional data, with two spatial and one spectral axes (x, y, λ). The spatial coordinates represent pixels corresponding to physical points on the object. The spectral dimension describes the intensity of either the reflected or the emitted light per wavelength at each pixel position. One of the recent trends in HSI development is the enhancing of regular 3D data with a fourth—either spatial (x, y, z, λ) [6], temporal (t, x, y, λ) [7], or spectral $(\lambda_{ex}, x, y, \lambda_{em})$ [8, 9, 10, 11] axis. Spectral enhancement of data consists of capturing 3D autofluorescence hyperspectral images, called datacubes, under different excitation conditions (by illuminating the object with monochromatic light of different wavelengths), then assembling the data into a 4D dataset. The idea behind this is to excite as many fluorophores as possible, which have different excitation profiles. In a single wavelength excitation HSI, in contrast, relevant fluorophores might remain unrevealed.

HSI has been applied to various biomedical problems, including: tumor detection and classification [12]; retinal biomarkers evaluation for the detection of preclinical Alzheimer's disease [13], visualization of skin complications in diabetes mellitus at early stages [4], diagnosis of Hirschsprung disease [14], detection of nerve injury caused by nerve compression in a chronic constriction nerve injury model [15]. HSI or equivalent techniques have also been applied to the nerve differentiation problem in the surgical context. Schols *et al.* [16] used diffuse reflectance within 350–1830 nm wavelength range in thyroid and parathyroid resections to discriminate between nerve, adipose tissue and muscle. Nouri *et al.* [17] used the reflectance from the mid-

*These authors contributed equally to this work

dle infrared range of 950–1660 nm to discriminate nerve from surrounding tissue in the context of parotidectomy intervention, where facial nerve is targeted. Maktabi *et al.* [18] used reflectance at 500–1000 nm and a supervised classification method to discriminate recurrent laryngeal nerve in thyroidectomy surgery. Barberio *et al.* [19] used similar imaging setup and machine learning methods to differentiate between the nerve and surrounding tissues, such as the artery, fat, muscle, skin and vein in an *in vivo* porcine model. Haugen *et al.* [20] and Throckmorton *et al.* [2] presented diffuse reflectance-based ratiometric approaches using different visible (VIS) to infrared (IR) range wavelengths for nerve visualization in *in vivo* rat models and human cadaver tissues. Tran *et al.* [21] used 400–1700 nm reflectance range for nerve versus fat, bone, and muscle differentiation in *ex vivo* human samples. Several deep learning techniques, specifically convolutional neural networks (CNNs) have been successfully applied to 3D HSI for biomedical applications, demonstrating their capability to extract spectral–spatial features for improved classification and segmentation tasks [22, 23].

In the majority of studies on nerve hyperspectral identification, diffuse reflectance-based imaging or spectroscopy was implemented. 4D autofluorescence HSI is currently underexplored for biomedical applications, in general, and nerve differentiation, in particular. [9, 10] recently explored nerve/ligament differentiation with 4D HSI, using traditional linear unmixing (LU) and CNN approaches. In particular, [10] introduced treating spectrally enhanced pixels as 2D images and applying a 2D CNN for their classification. However, there are two main questions with regard to 4D HSI. First, in contrast to 3D HSI, 4D acquisition is associated with higher time and technological costs; therefore, its superiority (if any) needs to be justified. Second, the optimal data configurations and processing approaches need to be determined, in order to maximally utilize the rich 4D information in the data. To address these questions in the context of nerve differentiation, we consider various 3D and 4D HSI configurations, combined with both LU and CNN approaches. A) We test whether and to what extent 4D HSI configurations improve classification accuracy over 3D HSI. B) The 'spectral pixels as images' approach [10] is compared against traditional 1D CNN applied to 3D configurations from 3D/4D HSI. We also explore a short-pass filter simulation to capture all excitation wavelengths used in 4D HSI, aiming to reveal fluorophores with distinct excitation–emission profiles while potentially reducing imaging time.

2. MATERIALS AND METHODS

2.1. Data Acquisition

Nerves and ligaments were isolated from bovine trotters purchased at the local market. The samples, and the resulting datasets (available at https://zenodo.org/communities/nar-sariph/), were denoted by the experiment date: *240618*, *240701*, *240718*, and *240730*. Throughout the experiments, including the imaging process, the tissues were kept in normal saline. A tunable light source (TLS130B-300X, Newport Corp, NJ) was used to illuminate the samples with monochromatic light ranging from 300 to 400 nm wavelengths, in 10 nm increments. Nuance FX imaging system (N-MSI-FX, CRi, Woburn, MA, USA) was used to acquire spectral images with bands from 420 to 720 nm, at 10 nm intervals, resulting in a 3D datacube per each excitation wavelength.

2.2. 3D and 4D Data Configurations

A hyperspectral dataset, containing individual 3D datacubes, each characterized by a specific excitation wavelength, is considered a 4D dataset. However, depending on the downstream analysis approach, different data configurations have been compiled from the same 4D dataset.

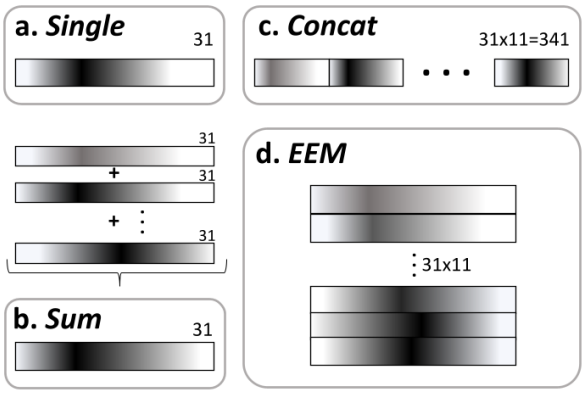

Fig. 1. Four configurations of spectral profiles extracted from each individual pixel of a 3D (a) or a 4D HSI dataset (b, c, d).

For the 3D analysis, the datacube corresponding to 360 nm excitation was used. This will be called the *Single* configuration. An element-wise sum of all datacubes is referred to as the *Sum* configuration. For the 4D analysis, two approaches were considered. In the first approach, all 3D datacubes were concatenated along their emission axis, resulting in spectrally augmented data for each pixel. This will be referred to as the *Concat* configuration. The resulting data structure is three-dimensional (x, y, λ_{em-aug}), although the data contains the information from the 4D dataset. In the second approach, excitation–emission matrices (EEMs) were generated for each pixel. This will be called the *EEM* configuration. In this case, the data structure remains four-dimensional $(x, y, \lambda_{ex}, \lambda_{em})$, where the last two axes represent the EEMs. Fig. 1 shows these four configurations and their dimensional differences.

3. COMPUTATIONAL SETUP

3.1. CNN Architecture

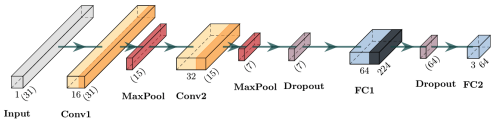

(a) 1D CNN

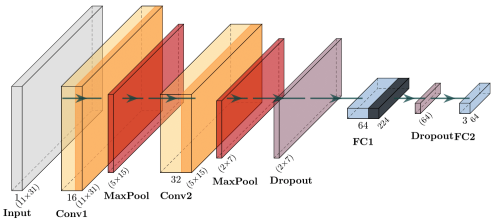

(b) 2D CNN

Fig. 2. CNN architectures used for pixel classification. (a) has been used for *Single*, *Sum* and *Concat* (with changed input size) data configurations, while (b) was used for *EEM*.

Two versions of CNN architectures are considered: 1D CNN for *Single, Sum, Concat* and 2D CNN for *EEM* data configurations. The proposed CNN architecture for 2D spectral data consists of two convolutional layers with ReLU activations, each followed by a max-pooling layer that reduces the spatial dimensions by half. The first convolutional layer applies 16 filters, expanding to 32 filters in the second layer, both with a kernel size of 3×3 and padding of 1. Then a dropout layer is used to prevent overfitting. The resulting feature map is flattened and passed through a fully connected layer with 64 units, then another dropout layer, before reaching the final output layer configured for three-class classification. For 1D CNN, the architecture is modified to use one-dimensional convolutional layers. The first convolutional layer applies 16 filters to 1D spectral data, followed by a max-pooling layer that reduces only the length dimension. The fully connected layer's input size is adjusted to match the flattened output from the final convolutional layer, making it compatible with 1D spectral data while still achieving three-class classification. Fig. 2 visualizes the described 1D and 2D CNN architectures designed for 3D (*Single, Sum, Concat*) and 4D (*EEM*) data structures, respectively.*

We trained the models for 100 epochs using cross-entropy loss and the Adam optimizer with an initial learning rate of 0.001. To assess the CNN's performance on each dataset, five distinct random train–test splits were considered. The analysis revealed that accuracy began to stabilize with as little as a 1% training set [10]. Thus, a 1% train, 99% test split is used in subsequent experiments to maintain high performance while keeping the training set minimal.

*Visualized with https://github.com/HarisIqbal88/PlotNeuralNet

3.2. Linear Unmixing

As a comparison baseline, the traditional HSI analysis approach of LU was applied. Nuance 3 software was used to perform LU on the *Single*, *Sum* and *Concat* configurations of the datasets. For comparability with the CNN approach, the same random pixels from the CNN classification were used to generate spectral libraries—average spectra for each class—from each configuration of the datasets. These libraries were then used for the unmixing. The resulting component images were processed for masks calculation, based on the maximum-value-component at each pixel position. These were then compared with manually generated reference masks to obtain accuracy values, representing the proportion of pixels identically assigned in analysis-derived and manually generated masks.

3.3. Statistical Analysis

A one-sided paired t-test was used to compare the mean results across different configurations within each analysis approach (CNN or LU). Additionally, a one-sided paired t-test was applied to compare each configuration's results between the two analysis approaches.

4. RESULTS AND DISCUSSION

Table 1. CNN classification accuracy (%) per sample, with four configurations: single 360 nm excitation cube, spectral sum, spectral concatenation, and EEM of 300–400 nm excitation cubes. Best result is in bold; second best—underlined.

Sample	*Single*	*Sum*	*Concat*	*EEM*
240618	87.86±0.76	89.32±0.41	<u>95.29</u>±1.10	**96.40**±0.47
240701	92.70±0.85	93.73±0.55	<u>98.00</u>±0.34	**98.86**±0.08
240718	96.88±0.09	98.06±0.30	<u>98.67</u>±0.06	**98.73**±0.06
240730	84.50±0.29	88.81±1.36	**95.15**±0.24	<u>95.14</u>±0.23

The CNN models yielded up to 98.9% overall accuracy in the task of nerve/ligament classification (Table 1). Moreover, they clearly showed a substantial improvement in tissue differentiation in favour of the 4D configurations (*Concat* and *EEM*), as demonstrated by the visualization of the masks overlaid on RGB renderings (Fig. 3). This statement holds true also numerically (Table 1). Both the *Concat* and the *EEM* configurations yielded a statistically significant improvement over the *Single* configuration ($p = 0.02$ in both cases). While the difference between *Concat* and *EEM* was not statistically significant ($p = 0.09$), a seemingly challenging portion of nerve tissue in the *240618* sample (probably due to some fascious substance) has been better classified in the *EEM* approach, as assessed visually (Fig. 3). The *Sum* configuration, even if not as good as the *Concat* and *EEM*, showed a performance statistically higher than the regular 3D

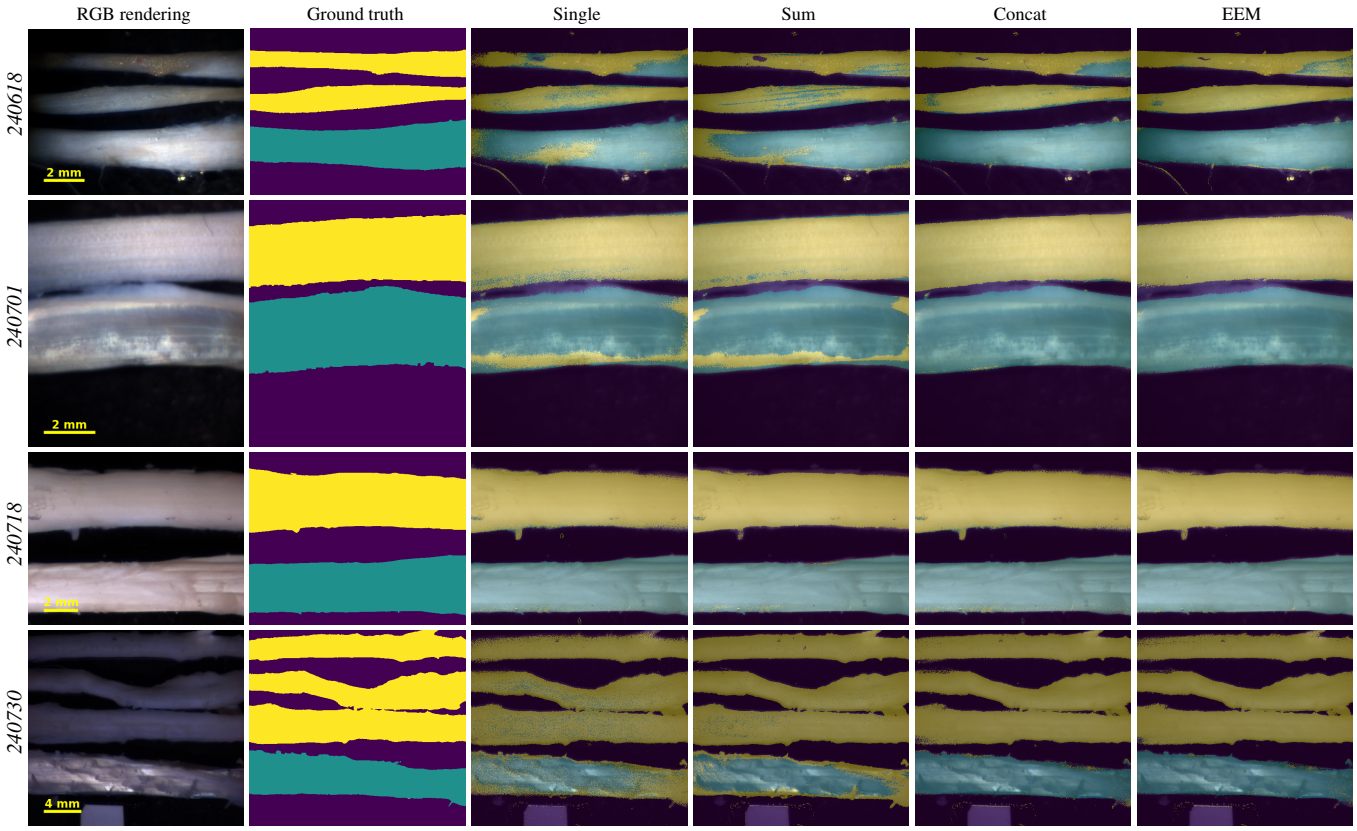

Fig. 3. Four datasets and their classification results overlaid on the RGB renderings. Background shade is purple, nerve is in yellow, ligament is in teal.

approach ($p = 0.04$). Additionally, average accuracy and Cohen's kappa coefficient were calculated. However, they provided no further insights, thus are not reported here.

Table 2. LU-based classification accuracy (%) per sample, with three configurations: single 360 nm excitation cube; spectral sum and spectral concatenation of 300–400 nm excitation cubes. Best result is in bold.

Sample	*Single*	*Sum*	*Concat*
240618	83.55±0.29	79.42±0.18	**88.60**±0.15
240701	89.53±0.07	89.42±0.12	**92.52**±0.23
240718	**88.06**±0.12	86.24±0.11	85.50±0.17
240730	72.50±0.39	73.77±0.33	**79.42**±0.29

LU achieved a maximum performance of 92.5% (Table 2). The comparison between data configurations showed no statistical difference within this analysis approach. Ultimately, the configuration-wise statistical comparison between CNN and LU approaches, showed that the CNN approach outperforms LU in case of all three configurations—*Single*, *Sum*, and *Concat*.

5. CONCLUSION

CNNs combined with autofluorescence hyperspectral imaging present a promising approach for intraoperative nerve identification. 4D imaging, with a 300–400 nm excitation wavelength range, significantly improves the classification accuracy, as compared to 3D data with 360 nm excitation only. The summed version of the 4D dataset performs slightly better than 3D, however with non-satisfactory accuracy. For all data configurations, CNN classification provides a higher-accuracy performance than LU. The limitations of the current work are twofold. One is the absorbance of light in our wavelength range of interest by biological fascious membranes. These can potentially prevent the excitation of target fluorophores, affecting the fluorescence that our approach is based on. However, given that our samples were not ideally isolated from fascia, CNN seems to overcome this limitation. Another limitation is the increased imaging time for 4D data acquisition. This may be overcome by finding and selecting a smaller, equally effective, set of excitation and emission wavelengths for image acquisition. This is a potential direction for future work. Ultimately, cross-sample validation of satisfactory performance has not yet been achieved. As a first step, imaging conditions standardization is necessary.

6. COMPLIANCE WITH ETHICAL STANDARDS

This study involved animal tissue purchased from a local abattoir; hence, no ethical approval was necessary.

7. ACKNOWLEDGMENTS

We are grateful to Fernando Villarruel, Tigran Soghomonyan, and Vahan Grigoryan for help in data acquisition, to Ani Avetisyan for consultations regarding Nuance FX software, and to Irina Voiculescu for advice in ideation of the approach. Financial support of the European Union (NAR-SAR-IPH-101087403) and Afeyan Family Foundation AUA Research Grant Program is gratefully acknowledged.

8. REFERENCES

[1] Thomas Kretschmer et al., "Iatrogenic nerve injuries," *Neurosurg Clin N Am*, vol. 20, no. 1, pp. 73–90, 2009.

[2] Graham A Throckmorton et al., "Label-free intraoperative nerve detection and visualization using ratiometric diffuse reflectance spectroscopy," *Sci Rep*, vol. 13, no. 1, pp. 7599, 2023.

[3] Caroline Chagnot et al., "Hyperspectral deep ultraviolet autofluorescence of muscle fibers is affected by postmortem changes," *J Agric Food Chem*, vol. 63, no. 19, pp. 4782–4789, 2015.

[4] Viktor Dremin et al., "Skin complications of diabetes mellitus revealed by polarized hyperspectral imaging and machine learning," *IEEE Trans Med Imaging*, vol. 40, no. 4, pp. 1207–1216, 2021.

[5] Sijia Jiang et al., "Bibliometric analysis of the current status and trends on medical hyperspectral imaging," *Front Med*, vol. 10, pp. 1235955, 2023.

[6] Jiaqiong Li et al., "4D line-scan hyperspectral imaging," *Opt Express*, vol. 29, no. 21, pp. 34835–34849, 2021.

[7] Isao Noda, "Two-dimensional correlation spectroscopy (2D-COS) analysis of evolving hyperspectral images," *Appl Spectrosc*, vol. 79, no. 1, pp. 77–86, 2025.

[8] Narine A Sarvazyan, "Hyper-excitation hyperspectral imaging system," 2023, Patent application #2023031963 (pending).

[9] Narek Chilingaryan et al., "4D hyperspectral imaging for intraoperative tissue classification," in *Medical Imaging 2025: CBI*. 2025, SPIE.

[10] Naira Matosyan et al., "Spectral pixels as images: CNN-based pixel classification of 4D hyperspectral data for nerve and ligament differentiation," in *Medical Imaging 2025: IP*. 2025, SPIE.

[11] Júlia Chaumel et al., "Autofluorescence of stingray skeletal cartilage: hyperspectral imaging as a tool for histological characterization," *Discov Mater*, vol. 1, no. 1, pp. 16, 2021.

[12] Samuel Ortega et al., "Hyperspectral imaging for the detection of glioblastoma tumor cells in H&E slides using convolutional neural networks," *Sensors*, vol. 20, no. 7, pp. 1911, 2020.

[13] Swati S More et al., "In vivo assessment of retinal biomarkers by hyperspectral imaging: early detection of Alzheimer's disease," *ACS Chem Neurosci*, vol. 10, no. 11, pp. 4492–4501, 2019.

[14] Marcos A Soares de Oliveira et al., "Diagnosing Hirschsprung disease by detecting intestinal ganglion cells using label-free hyperspectral microscopy," *Sci Rep*, vol. 11, no. 1, pp. 1398, 2021.

[15] Martin E Gosnell et al., "Autofluorescent imprint of chronic constriction nerve injury identified by deep learning," *Neurobiol Dis*, vol. 160, pp. 105528, 2021.

[16] Rutger M Schols et al., "Differentiation between nerve and adipose tissue using wide-band (350–1,830 nm) in vivo diffuse reflectance spectroscopy," *Lasers Surg Med*, vol. 46, no. 7, pp. 538–545, 2014.

[17] Dorra Nouri et al., "Hyperspectral interventional imaging for enhanced tissue visualization and discrimination combining band selection methods," *Int J Comput Assist Radiol Surg*, vol. 11, pp. 2185–2197, 2016.

[18] Marianne Maktabi et al., "Classification of hyperspectral endocrine tissue images using support vector machines," *Int J Med Robot Comp Assist Surg*, vol. 16, no. 5, pp. 1–10, 2020.

[19] Manuel Barberio et al., "Deep learning analysis of in vivo hyperspectral images for automated intraoperative nerve detection," *Diagnostics*, vol. 11, no. 8, pp. 1508, 2021.

[20] Ezekiel J Haugen et al., "Measurement of rat and human tissue optical properties for improving the optical detection and visualization of peripheral nerves," *Biomed Opt Express*, vol. 14, no. 6, pp. 2839–2856, 2023.

[21] Minh Ha Tran et al., "Nerve detection and visualization using hyperspectral imaging for surgical guidance," in *Medical Imaging 2024: CBI*. 2024, vol. 12930, p. 129302A, SPIE.

[22] Jonghee Yoon, "Hyperspectral imaging for clinical applications," *BioChip J*, vol. 16, no. 1, pp. 1–12, 2022.

[23] Jignesh S Bhatt and Manjunath V Joshi, "Deep learning in hyperspectral unmixing: A review," in *IGARSS 2020*. 2020, pp. 2189–2192, IEEE.